Comparison of a hybrid model and experimental measurements for a dielectric-coated coaxial ECR thruster

Álvaro Sánchez-Villar, Federico Boni, Victor Désangles, Julien Jarrige, Denis Packan, Eduardo Ahedo, Mario Merino

PAPER • **OPEN ACCESS**

Comparison of a hybrid model and experimental measurements for a dielectric-coated coaxial ECR thruster

To cite this article: Álvaro Sánchez-Villar *et al* 2023 *Plasma Sources Sci. Technol.* **32** 014002

OPEN ACCESS
IOP Publishing
Plasma Sources Science and Technology
Plasma Sources Sci. Technol. **32** (2023) 014002 (12pp)
https://doi.org/10.1088/1361-6595/acb00c

Comparison of a hybrid model and experimental measurements for a dielectric-coated coaxial ECR thruster

Álvaro Sánchez-Villar[1,3,*], Federico Boni[2], Victor Désangles[2], Julien Jarrige[2], Denis Packan[2], Eduardo Ahedo[1] and Mario Merino[1]

[1] Equipo de Propulsion Espacial y Plasmas (EP2), Universidad Carlos III de Madrid, Leganés, Spain
[2] DPHY, ONERA, Université Paris-Saclay, F-91123 Palaiseau, France

E-mail: asanche2@pppl.gov

Received 15 November 2022
Accepted for publication 4 January 2023
Published 26 January 2023

Abstract

Electrostatic probe and thrust balance measurements of a coaxial electron-cyclotron-resonance plasma thruster with magnetic nozzle are compared against numerical simulations of the device that solve self-consistently the plasma transport problem with a hybrid particle-in-cell/fluid approach and the microwave electromagnetic fields using mixed finite elements. A simple phenomenological anomalous transport model similar to those used in Hall thruster modeling is applied. Reasonable average relative errors are reported on the ion current density (8.7%) and plasma density (12.8%) profiles along the plume. Good agreement is found in terms of relative errors on thruster performance parameters as the 90%-current divergence angle (0%–3%), utilization efficiency (3%–10%), peak ion energy (9%–15%), and energy efficiency (2%–17%). The comparison suggests that enhanced cross-field diffusion is present in the plasma. Differences in the experimental and numerical behavior of electron temperature point to the areas of the model that could be improved. These include the electron heat flux closure relation, which must correctly account for the axial electron cooling observed.

Keywords: ECRT, electrodeless plasma thruster, PIC, fluid, electromagnetic

(Some figures may appear in colour only in the online journal)

1. Introduction

The electron cyclotron resonance thruster (ECRT) belongs to the family of electrodeless plasma thrusters with magnetic nozzle, together with the helicon plasma thruster (HPT)[1, 2] and the variable specific impulse magnetoplasma rocket [3]. The first research efforts on the ECRT concept took place in the 1960s [4, 5] and the late 1980s [6]. These first prototypes consisted of a waveguide with a microwave generator and a cylindrical ionization chamber with a propellant gas supply, separated by a dielectric window, and an essentially-axial applied magnetic field that diverged outside of the device to form a magnetic nozzle. The magnetic field allows the propagation of the microwave into overdense plasma and generates an electron cyclotron resonance (ECR) region inside the ionization chamber, which serves as the main power delivery mechanism.

Later works [7, 8] developed and characterized a coaxial version of the ECRT, where the waveguide is replaced by a coaxial line whose core is terminated in a rod, immersed in the ionization chamber. This new version has been seen to generate high ion energy beams (up to 300 eV) and thrust levels up to 1 mN at low powers (below 50 W of absorbed power). The experimental study of this device continues in Europe [9–13] and in the USA [14–16]. Of particular interest to the present study is the work of Hepner *et al* [16], who reported evidence supporting the existence of wave-enhanced cross-field transport in the magnetic nozzle of a coaxial ECRT similar to the one investigated here. Those authors identify a

[3] Present address: Princeton Plasma Physics Laboratory, 100 Stellarator Rd, Princeton, NJ 08540, United States of America
[*] Author to whom any correspondence should be addressed.

lower hybrid drift instability along the plume, which would reduce the effective Hall parameter by several orders of magnitude, enhancing the radially-outward electron transport, which would ultimately increase plasma losses and increase plume divergence.

Despite the extensive experimental work carried out on the ECRT, the modeling and simulation efforts remain scarce, in part due to the complexity of the involved physics. A 0D global model simulating the perpendicular electron energy distribution function using diffusion coefficients in a Fokker–Planck equation was tuned to reproduce the experimental ion ejection energy trend within a parametric study and to stress the importance of the backplate secondary electron emission influence [17]. An analytical quasi-1D model designed for HPTs was adapted to the ECRT case and applied to estimate successfully the overall thruster performance for high flow rate values (the model was less successful for low flow rates) [18]. However, the model underestimated the electron temperature and lacked modeling of both cross-field diffusion as well as radio-frequency source/plasma power coupling. A more complete two-dimensional axisymmetric model of the ECRT including these two last features has been developed and applied recently to obtain coupled simulations of the plasma wave interaction and the plasma transport [19]. The plasma transport is modeled using the particle-in-cell (PIC) method for the heavy species (i.e. neutrals and ions) and a fluid scheme for the magnetized electrons [20–22]. Turbulent-based cross-field transport of electrons was modeled empirically. The electromagnetic response of the plasma is modeled with Maxwell inhomogeneous wave equation and a collisional cold plasma dielectric tensor formulation [23], solved in the variational form using mixed finite elements [24, 25].

Crucially, this ECRT model must be validated against experimental data to assess the validity of its assumptions and the overall simulation approach, and to identify areas of improvement. This requires a dedicated test campaign to measure the steady-state plasma profiles and the thruster performance figures, against which the model predictions can be compared. Capturing these parameters reliably is a challenging task, complicated by the limited access to certain plasma regions such as the interior of the ionization chamber, the inherent uncertainty associated to plasma measurements, and the repeatability of the thruster firings.

The main objective of this work is to perform a first validation of the ECRT model presented in [19] by carrying out a comparison of its results with experimental measurements of thrust, plasma density, ion current density, electron temperature, electrostatic potential, and ion energy distribution function (IEDF), in a wide plume region of the ECRT prototype investigated in [10], using different types of plasma diagnostics. Angular and axial scans of these properties are compared with simulation results.

A tunable, one-parameter model of cross-field electron diffusion, which is based on existing empirical models of anomalous transport in Hall-effect thrusters (HETs) [21, 26–28], is used to fit the simulation results to the experimental data or, in other words, to estimate the real values of the cross-field diffusion coefficients. The enhanced diffusion decreases the effective Hall parameter and causes a larger radially-outward transport of plasma, in qualitative agreement with the observed transport in [16]. It will be shown below that certain augmented diffusion is needed to reproduce the measurements, supporting the idea that some form of anomalous transport is also present in ECRTs.

The rest of the paper is structured as follows. Section 2 describes the thruster configuration, experimental setup, and simulation model. Section 3 presents and discusses the experimental results and their comparison with the simulations. Finally, section 4 gathers the main conclusions of this work.

2. Methodology

This section details the thruster prototype and the facilities and diagnostic techniques used for the validation. Additionally, a brief overview of the simulation model presented in [19] is provided.

In the following, the right-handed orthonormal magnetic vector basis $\{1_\perp, 1_\parallel, 1_\theta\}$ displayed in figure 1(a) is used, where $1_\perp$ and $1_\parallel$ represent the perpendicular and parallel directions to the local magnetic field vector $\boldsymbol{B}$ in the meridional plane, and 1_θ is the azimuthal direction. Coordinates (z, r) refer to the cylindrical coordinates about the thruster centerline, while (ρ, ψ) are the polar coordinates of the angular measurement system, with origin at the center of the thruster backplate.

2.1. Thruster configuration

The ECRT prototype developed at ONERA since 2010, and more recently within the framework of the H2020 MINOTOR project [9, 12, 13, 29, 30], has been used as the reference thruster for the study.

Figure 1(a) shows the simulated meridian cross section of the plasma source and plume, and figure 1(b) presents the ECRT prototype in operation. The prototype consists of a $L = 2$ cm long coaxial ionization chamber with $R = 1.375$ cm outer radius and 0.115 cm inner radius, connected to a coaxial feed line. The inner and outer conductors are made of metal and a boron nitride (BN) backplate, transparent to microwave power, is located at $z = 0$. The magnetic field is provided by an annular permanent magnet placed at the back of the ECR source, so that the magnetic field intensity reaches 875 G inside the ionization chamber, corresponding to an electron cyclotron frequency of 2.45 GHz. The thruster is powered by a microwave generator operating at this frequency. The microwave power deposited in the plasma (P_a) is kept constant by measuring the injected and reflected power at the output of the microwave generator. The thruster is fed with xenon mass flow rate $\dot{m}$ with a radial injection configuration [31].

For this study, the thruster inner and outer walls are coated with BN spray in order to be compatible with the dielectric boundary conditions of the simulations. The antenna is made of graphite with a 50–100 μm pyrolytic BN coating from Stanford Advanced Materials. The operating conditions are fixed at $P_a = 30$ W and $\dot{m} = 2$ sccm, though this is not the optimum identified in previous studies [10]. Although similar

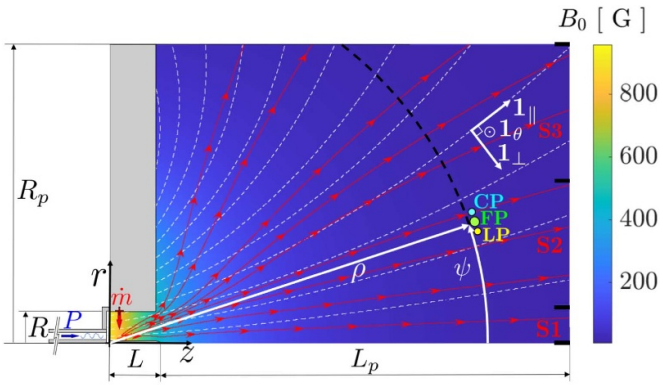

(a)

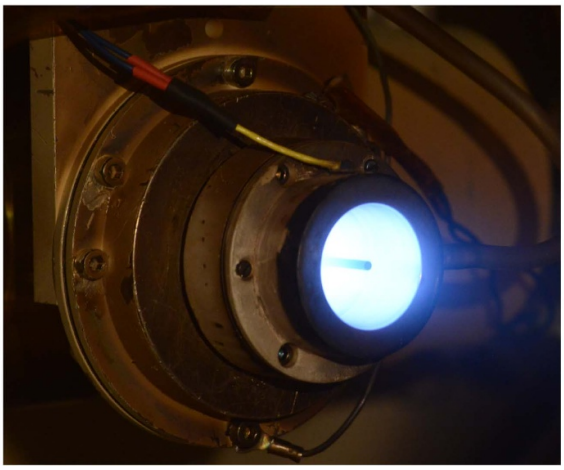

(b)

Figure 1. (a) ECRT simulation domain, with plume dimensions $L_p = 18$ cm and $R_p = 13$ cm, magnetic field intensity (colormap), magnetic field lines (dashed white), local magnetic vector basis (white), selected Xe^+ streamlines for simulation case $\alpha_t = 0.05$ (solid red) and segments at the end boundary (black) defining the regions used for IEDF averaging, detailed in section 3.2. Additionally, the position of the plasma probes as a function of the coordinates (ρ, ψ) in the experimental setup discussed in section 2.2 is sketched. (b) Photograph of the ECRT prototype operating in the ONERA-B09 facility.

performances in terms of thrust F, thrust efficiency η_F and ion beam current I_b have been obtained with the dielectric wall thruster compared to the conductive wall thruster at 2 sccm and 30 W, a higher variability has been observed in terms of ion current density j_i and electron density n_e. Finally, it has been noticed that the experimental setup in the B09 vacuum chamber at ONERA (the one used in this study) tends to lower the thruster efficiency with respect to the B61 larger vacuum chamber (used in [10]). The relative figures are summarized in table 1 and their repeatability is assessed in terms of relative standard deviation. The higher variability observed in the maximum ion current measured on the dielectric wall thruster compared to the conductive wall thruster is understood as an ageing effect of the coating during thruster operation. However, while the maximum ion current density values differ, both the ion beam current and the normalized ion current density profiles are essentially similar. Given this similarity, we choose to carry out the comparison with the numerical results in terms of normalized profiles, rather than the peak values of specific experimental data.

2.2. Experimental setup

As mentioned above, experiments are carried out in the ONERA-B09 facility, a stainless-steel cylindrical vacuum chamber of 2 m in length and 0.8 m in diameter. The pumping system consists of three turbomolecular pumps and one cryogenic pump, yielding a total pumping speed of 13 000 $1\,s^{-1}$ for xenon, with a base pressure of 10^{-7} mbar-N_2. The typical pressure when injecting 2 sccm of xenon is in the order of 2.5×10^{-6} mbar-Xe. Slightly higher pressures are measured during thruster operation due to increased chamber wall outgassing under the effect of high-energy ions. The first 60 cm of the vacuum chamber were covered in dielectric Kapton to mimic the dielectric boundary conditions used in the numerical model described in the next section.

The microwave power line consists of VAUNIX LMS-402D signal generator and a Microwave Amps Ltd power amplifier. The forward and reflected power to and from the thruster is measured with two LB478A (LadyBug Technologies) power sensors and directional couplers. Power losses through the feeding line are measured before the test campaigns to compute the total absorbed power by the thruster. Thrust measurements are performed with the thrust balance developed at ONERA [10], which is a pendulum balance with a frictionless pivot.

Plasma parameters are collected along angular and axial profiles in the plume region. The diagnostics are performed with three different probes constructed in-house, plus a commercial ion analyzer. The electron density n_e is measured with a microwave resonant probe and a Langmuir probe (LP). The latter also allows the electron temperature T_e and the electrostatic potential ϕ to be measured. The resonant probe is a curling probe, called CP700 in [32], consisting of a 35 μm-thick spiral copper resonator of 106 mm in length, etched on a 0.5 mm-thick RO4003 sheet. The local electron density is calculated following the plasma permittivity [32]. The LP consists of a tungsten wire of 150 μm in diameter and 5 mm in length. The bias voltage at the probe tip is swept from -100 V to $+100/+120$ V, depending on the probe distance to the thruster. The collected current is measured through a 6 kΩ-shunt resistance. Data are post-processed using the Druyvestein method [33] and OML theory to determine electron density and temperature. A low discrepancy in the results is obtained from the two post-processing methods. The ion current density j_i is measured with a gridded Faraday probe (FP), which consists of a stainless steel collector of 6 mm in diameter biased at -350 V. The grid, placed between the plasma and the collector, is electrically-floating and limit the increase of the collection area of the probe when increasing its bias voltage [10]. The low bias potential value of the collector is necessary to reach the ion saturation current in the central part of the thruster plume due to high electron temperatures. The collected ion current is measured through a 33 kΩ-shunt resistance. The Faraday and Langmuir signals are recorded on a National Instruments DAQ board (NI BNC-2110). Error

Table 1. Comparison of performance figures and reproducibility of probe measurements of the conductive and dielectric thruster configurations at 30 W. Measurements indicated with * are taken at $\rho = 26$ cm from the backplate; the rest are taken at 16 cm.

Wall surface	$\dot{m}$ (sccm)	F (μN)	η_F (%)	E_i (eV)	$\overline{I_b}$ (mA)	$\overline{j_{i,max}}$ (Am^{-2})	$\overline{n_{e,max}}$ ($\times 10^{15}$ m^{-3})	RSD(I_b) (%)	RSD($j_{i,max}$) (%)	RSD($n_{e,max}$) (%)
Conductive	1	565	5.5	200	45	0.9*	—	—	—	—
Conductive	2	620	3.3	91	58	1.5*	—	12	10*	—
Dielectric	2	601	3.1	65	62	7.5	3.2	12	18	9.5

bars, accounting for measurement uncertainties for the curling, Faraday, and LP, are estimated as detailed in [32, 34, 35], respectively. The presented error bars do not account for thruster operation variability.

The IEDF is measured with a PSM003 Hiden Analytical ion analyzer, which faces the thruster and is mounted at approximately 1.7 m from the thruster exit plane.

The angular profiles are obtained with the probes mounted on a motorized rotational stage with the rotation axis centered at the thruster backplate, as shown in figure 1(a), following the polar coordinates (ρ, ψ). The profiles are taken 16 cm downstream from the backplate, and the angle ψ is varied between $-70°$ and $70°$. FPs are oriented such that the collecting (i.e. measuring) surface normal is along the ρ-direction for all ψ angles. For the axial profiles, the probes are moved using motorized translational stages, allowing the measurement along the z axis defined in figure 1(a).

2.3. ECRT model

The model detailed in [19] allows to compute steady-state solutions of the coupled plasma transport and electromagnetic plasma response in ECRTs. The reader is referred to that work for the details of the model and its numerical implementation. In the following, only its main aspects are reviewed.

The simulation domain corresponds to that shown in figure 1(a). The source with dimensions R and L is simulated in a domain with a plume of length $L_p = 18$ cm and radius $R_p = 13$ cm. The model is composed of three main modules: a PIC module to simulate the heavy species (ions and neutrals), a fluid module for the electrons, and a full-wave module to compute the electromagnetic fields.

The PIC module uses a structured grid mesh where the electrostatic field is computed and the magnetostatic field is interpolated. Macroparticle trajetories are integrated using a 3D Cartesian leap-frog algorithm for advancing a time step Δt, and their position is then projected to the meridian plane of the axisymmetric simulation. A boundary cross checking algorithm identifies the macroparticles leaving the domain. The PIC-module also includes the effect of (i) ionization (single, double, and single to double) by electron bombardment, and (ii) neutral accommodation and re-emission and ion recombination at the walls. A weighting algorithm computes the integrated macroscopic properties on the PIC mesh of characteristic cell size of 1 mm inside the thruster and few millimeters in the plume, every ion time step (50 ns). Roughly 500 macroparticles per cell are set in the simulation as target for the population control algorithm. Time-averaging of the weighted properties is used to limit numerical noise.

The electron fluid module considers the continuity equation and the electron momentum, energy, and heat flux equations with appropriate source terms for ionization, excitation and elastic electron collisions with ions and neutrals. The closure of the hierarchy of fluid equations is done at heat flux level. The system of equations is solved numerically using the finite volume method and a time marching scheme. A magnetic field-aligned mesh is used to reduce numerical diffusion [36]. Plasma properties are interpolated between the Cartesian PIC mesh and the magnetic field aligned mesh as needed. Around the material walls, a sheath module solves a planar unmagnetized collisionless kinetic model of the Debye sheaths [22], including secondary electron emission and non-Maxwellian features of the electron velocity distribution function.

As explained in the Introduction, a simple phenomenological model of turbulent anomalous transport [21] is included, which increases the perpendicular diffusion of electron momentum and energy. The model is based on an empirical parameter α_t representing the average turbulence level. Specifically, this means that an extra force, $\boldsymbol{F}_{ano} = \alpha_t B_0 j_{\theta e} 1_\theta$, and an extra heat flux, $\boldsymbol{Y}_{ano} = -\alpha_t B_0 q_{\theta e} 1_\theta$, are introduced in the electron fluid equations. A multi-parametric version of this approach is being used successfully in modeling HET axisymmetric discharges [21, 22]. Here, an α_t homogeneous over the simulation domain is applied as a first approach to tackle the anomalous transport in ECRTs. Simulations will find $\alpha_t = 0.035$–0.08 as a suitable range, which is similar to the one found in HET simulations.

If $\omega_{ce} = eB/m_e$ is the electron cyclotron frequency and ν_e is the electron overall collisionality with ions and neutrals, a non-zero α_t reduces the Hall parameter from $\chi = \omega_{ce}/\nu_e$ to [22]

$$\chi_{eff} = \frac{\chi}{\sqrt{1 + \alpha_t \omega_{ce}/\nu_e}} \simeq \sqrt{\frac{\chi}{\alpha_t}}. \tag{1}$$

In the ECRT investigated here the values of χ are found to vary approximately in the range $[10^3$–$10^5]$. For α_t chosen in the range [0.01–0.1] the values of χ_{eff} are decreased by one or two orders of magnitude. This effect is comparable to the quasilinear wave-driven decrease of χ_{eff} computed in [16], and also to the decrease in χ_{eff} applied to the magnetic nozzle simulations in [37], where $\chi \sim 10^6$ is artificially capped to $\chi_{eff} = 3 \times 10^4$.

The PIC and the electron fluid modules enable computing the slow plasma dynamics inside the thruster and in the magnetic nozzle. The weighted ion and electron densities on the underlying mesh are used to compute the quasi-static part of

the electric field. Plasma sheaths are modeled at the walls. The walls are treated as dielectric surfaces, and the sheath potential fall is computed accordingly to maintain the local charge current balance. An algorithm watches the fulfilment of Bohm's condition at the sheath entrance and corrects the presheath voltage initially (i.e. the voltage in the cells near the walls) to enforce it until it is automatically satisfied in subsequent time steps [21].

Lastly, the (fast) fields in the plasma are computed using an electromagnetic wave module, which solves Maxwell's inhomogeneous wave equation in its variational form, with a cold-plasma collisional dielectric tensor model [23]. The module utilizes Galerkin's finite element method applying a mixed vector and nodal finite element discretization scheme [25, 38]. The dielectric tensor is computed locally based on the magnetic field, and the electron density and collisionality obtained by the transport modules. Electromagnetic fields are excited by introducing the transverse electromagnetic mode in the coaxial line at the back end of the thruster, which then accesses the plasma source through the dielectric window. The effect of the thin dielectric coating on the metallic thruster walls is neglected in the wave propagation problem, and the thruster walls are treated as perfect electric conductors within the electromagnetic module. Most of the power is absorbed at the ECR, and the electromagnetic power reaching the open boundaries of the domain is negligible. The model computes the electromagnetic power density distribution deposited in the plasma, which enters as an input in the electron energy equation. The electromagnetic fields are updated every 10^4 ion time steps until convergence to a stationary, self-consistent solution is achieved. This typically requires a total of 3–4 electromagnetic field updates and a total of 1.5–2 ms simulation time.

3. Results and discussion

In this section, we present the experimental results obtained in the near plume of the ECRT prototype and find the best fitting of cross-field diffusion for the numerical simulations.

3.1. Ion current density and electron density

Figure 2 shows the comparison between the numerical and experimental angular profiles for both the ion current density perpendicular to the FP collection surface j_i, normalized with its peak value, and the electron density n_e, at $\rho = 16$ cm from the thruster backplate. Figure 3 shows the comparison along the thruster symmetry axis ($r = 0$). Numerical simulations are carried out for three different values of the turbulent anomalous transport parameter α_t (0.035, 0.05 and 0.08). Reasonable agreement is found on both the normalized j_i and n_e profiles. It is noteworthy that also the lateral plume wings (which show the presence of a low density plasma on angles higher than 20°) are well reproduced by the simulation results for both j_i and n_e.

The (integrated) ion beam current $I_b(\psi_{max})$ is computed from $j_i(\psi)$ as

$$I_b(\psi_{max}) = \pi\rho^2 \int_{-\psi_{max}}^{\psi_{max}} j_i(\psi)\sin(|\psi|)\mathrm{d}\psi. \quad (2)$$

The ion beam current I_b is compared for $\rho = 16$ cm and $\psi_{max} = 45°$, as 90° is not accessible with neither the experiments nor the chosen simulation domain. The experimental value of $I_b($ is 41.4 ± 4.2 mA, while 48.4, 43.0 and 37.1 mA are obtained for simulations with $\alpha_t = 0.035, 0.05,$ and 0.08, respectively.

The results obtained by the model suggest that at least some anomalous cross-field diffusion is needed to reproduce the profiles found experimentally. The simulation with the lower value of α_t displays a double-peaked angular profile, not observed experimentally. Values around $\alpha_t = 0.05$ seem to yield an adequate fit of these experimental results.

The overall effects of increasing α_t are (i) decreasing the gradients in the perpendicular direction, resulting in a single-peaked angular profile, and (ii) decreasing the peak value of j_i and n_e. In other words, the enhanced cross-field transport acts as to homogenize the plasma quantities in the perpendicular direction by allowing more plasma to diffuse radially-outward, resulting in smoother gradients in this direction and increasing the plume divergence. The larger plume divergence leads to a faster decrease of plasma density, ion current density, and other properties in the axial direction, as shown further below.

Axially, the three simulations exhibit a similar behavior in the region where measurements are available, and show a good match with them, as shown in figure 3. A slightly faster expansion rate is suggested by the experimental measurements of n_e than the one predicted by the simulations. The major differences among simulations arise further upstream, and are due to the varying plume divergence angle, which is larger as α_t is increased, and results in a faster-decaying j_i and n_e in the axial direction.

To gain further insight into the behavior of the simulations upstream, figure 4 displays the angular profiles of the electron density at $\rho = 8, 12,$ and 16 cm, for the different cases of α_t presented. A double-peaked angular profile is predicted by all simulations upstream to some extent, and this feature becomes more evident and survives longer downstream the smaller the value of α_t. The depression in the central part of the plume is attributed to the presence of the inner rod inside the thruster ionization chamber, which is seen to lower the plasma density in its wake, until cross-field diffusion refills this region and a single-peaked profile forms. As cross-field diffusion increases with increasing α_t, this concavity is erased away earlier in the expansion. Double-peaked profiles have been observed experimentally in the ion current density measurements for similar coaxial ECRT prototype versions and lower mass flow rates [10, 39]. This feature has also been reported in other thrusters with magnetic nozzles, but are likely due to other reasons as a radially-uneven power absorption profile [2, 40].

3.2. Ion energy

Figure 5 shows the measured IEDF by the ion analyzer, located at the end of the vacuum chamber. The distribution features an asymmetric peak at approximately 65 eV, and a smaller (∼5%)

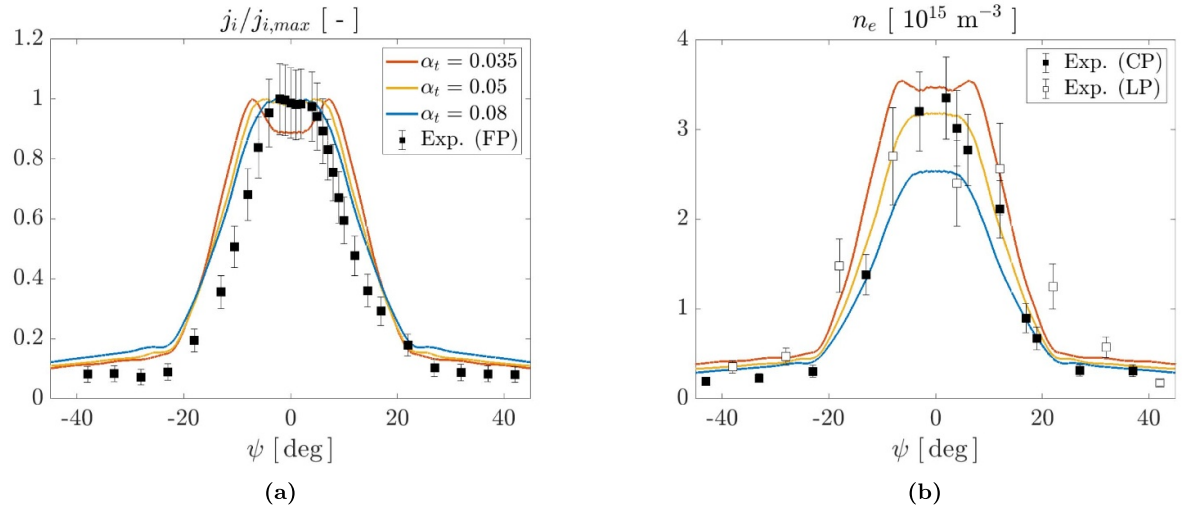

Figure 2. Angular profiles of (a) normalized ion current density and (b) electron density at $\rho = 16$ cm. Numerical results (solid lines) for different anomalous transport coefficients are shown against experimental measurements (scatter symbols).

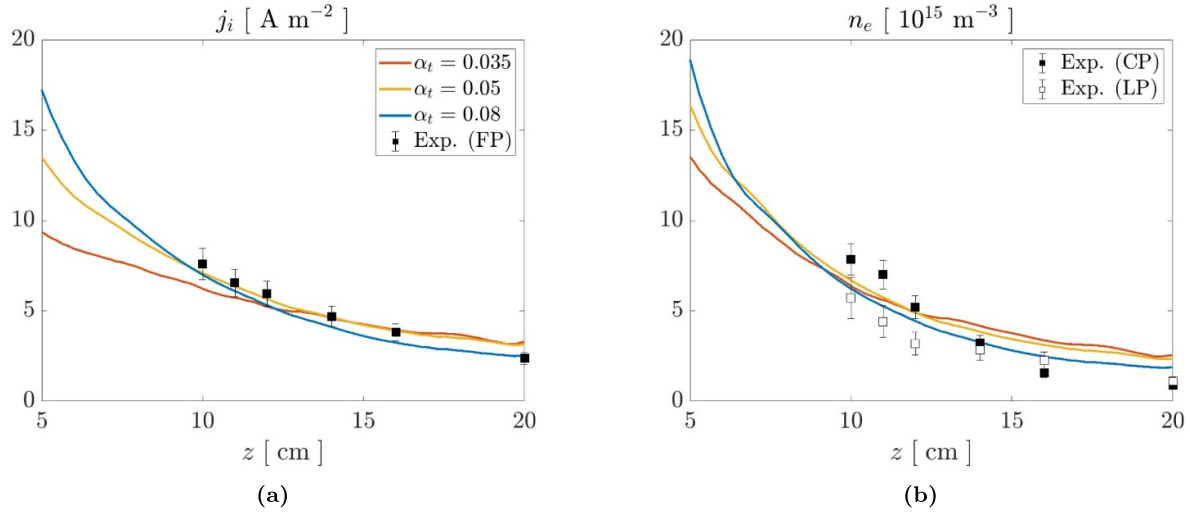

Figure 3. Axial profiles of (a) the ion current density and (b) electron density along the magnetic nozzle expansion at $r = 0$ ($\psi = 0$). Numerical results (solid lines) for different anomalous transport coefficients are shown against experimental measurements (scatter symbols).

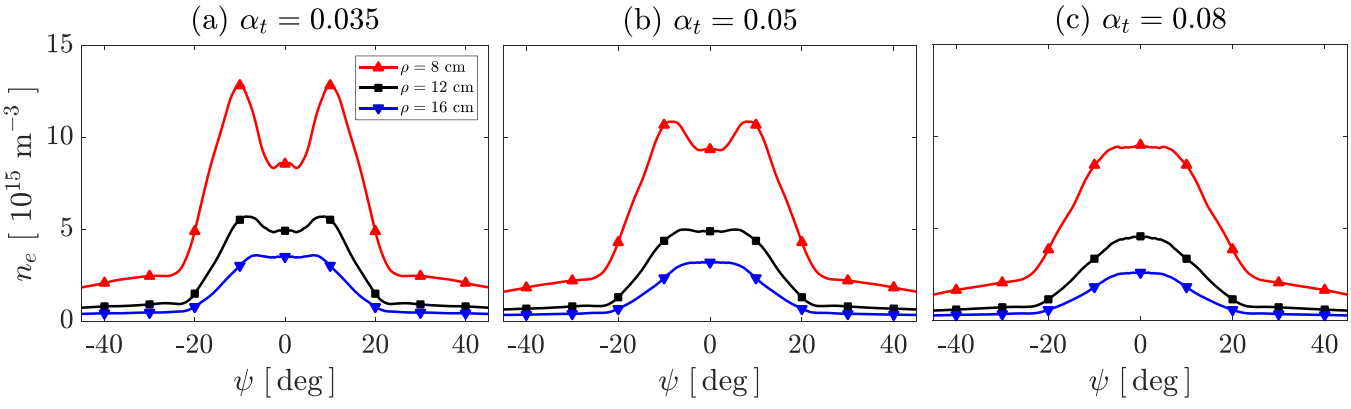

Figure 4. Numerical angular electron density n_e profiles at different ρ, for (a) $\alpha_t = 0.035$, (b) $\alpha_t = 0.05$ and (c) $\alpha_t = 0.08$ at 2 sccm −30 W.

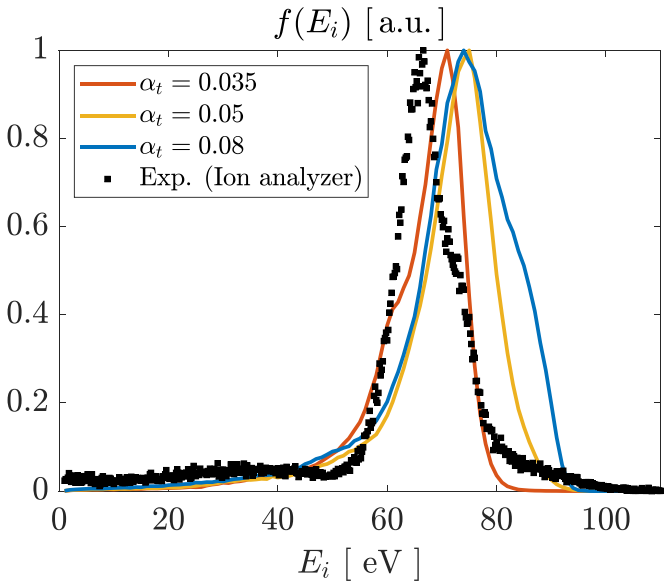

Figure 5. Comparison of the IEDF of Xe^+ measured experimentally with the ion analyzer (square scatter points) to the one obtained numerically at the end of the simulated plume for the cases with $\alpha_t = 0.035$, 0.05, and 0.08.

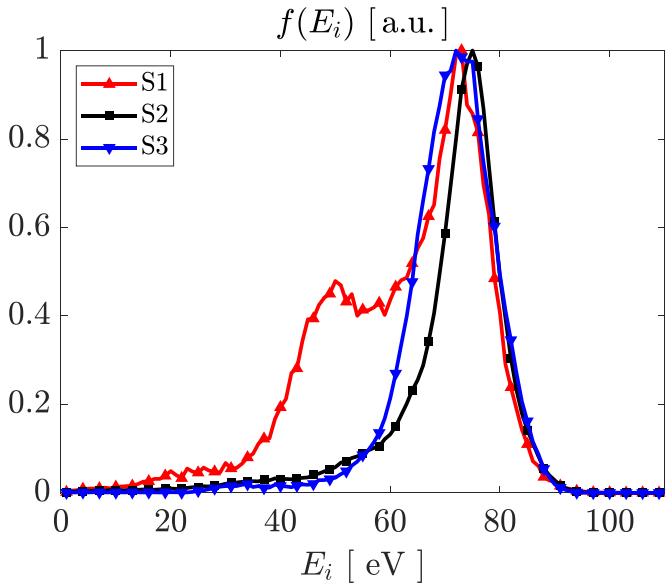

Figure 6. Comparison of the IEDFs of Xe^+ for the case of $\alpha_t = 0.05$ at three different regions, corresponding to the regions centered around the end of streamlines S1 (red), S2 (black) and S3 (blue) shown in figure 1(a).

secondary bump at around 30 eV. Figure 5 also depicts the numerical weighted-averaged IEDF of Xe^+ exiting the simulation domain through its end boundary (18 cm downstream from the thruster exit, which is less than the vacuum chamber length). The IEDF averaging is performed over the end boundary panels, with a weight corresponding to the panel area. The peak ion energy for the simulation cases are 71, 75 and 74 eV for $\alpha_t = 0.035, 0.05, 0.08$, respectively. This is a 9%–15% difference with respect to the measured peak.

As the experiment takes its measurements further downstream than the end of the simulated plume, a slightly higher ion energy is expected in the test results than in the simulations. However, the experimental peak ion energy is lower than the numerical one, meaning that the simulations marginally overestimate the ion energy. As the ion energy and the electrostatic potential drop in the plume are closely related to the electron temperature, the difference in peak values is a first indication that the simulation may be overestimating T_e, as further discussed in section 3.4. However, part of this difference could also be attributed to the background pressure effect present in the experiment and which is absent in the simulation. Indeed, Wachs and Jorns [15] recently showed laser induced fluorescence measurements in a similar ECRT device to the one analyzed in this work, featuring a 37% ion energy drop for an increase in background pressure from 1.3×10^{-6} to 3.5×10^{-5} mbar-Xe. Notwithstanding this, the width of the IEDF primary peak is in good agreement with the experimental measurement, especially for the lower values of α_t. The effect of α_t in the IEDF is otherwise minor.

Figure 6 shows the IEDF for the simulation with $\alpha_t = 0.05$ at three different radii. The IEDF averaging is carried out over the neighboring boundary panels on three radii spans [0–1.5, 1.5–7, 7–13] cm. These regions are selected so that their weighted-average radii correspond with streamlines S1, S2 and S3 at the end boundary (see figure 1(a)). It can be noticed that the peak ion energy is barely affected by the radial location. However, a low energy tail of approximately 45% of the peak value is found around 45–50 eV at S1, closest to the thruster axis. The existence of this lower energy ion population in the central part of the plume is explained as follows. Figure 7 shows the evolution in this simulation of the electrostatic potential ϕ, the singly-charged xenon ions (Xe^+) mean kinetic energy $mu_i^2/2$ where u_i is the macroscopic fluid velocity, the Xe^+ mean total energy $H_i = mu_i^2/2 + e\phi + 3T_i/2$, and the volume ionization source S_{ion}, along the arc length s of the three representative ion streamlines shown in figure 1(a).

In an ideally collisionless, steady-state expansion, the bulk ion total energy is conserved along streamlines. However, in the simulated ECRT plume, significant ionization takes place in the acceleration region and near plume, and results in newly generated ions with lower kinetic energy, which increase the width of the IEDF and the ion temperature T_i, and decrease the mean total ion energy of the ion population along that streamline.

The ionization source term, representing the source of singly-charged ions generated by simple ionization per unit time, is proportional to the neutral and plasma densities and the ionization reaction rate, which depends on the local electron temperature [41]. It has been previously observed that the electron temperature on each streamline is dependent on the electromagnetic radial power absorption profile upstream [19]. Moreover the neutral density in the near plume is larger near the axis than in the periphery. As a result, S1 features greater ionization and the mean total ion energy decreases down to approximately 65 eV near the thruster, while ion temperature increases mildly to $T_i = 1.5$ eV. This explains

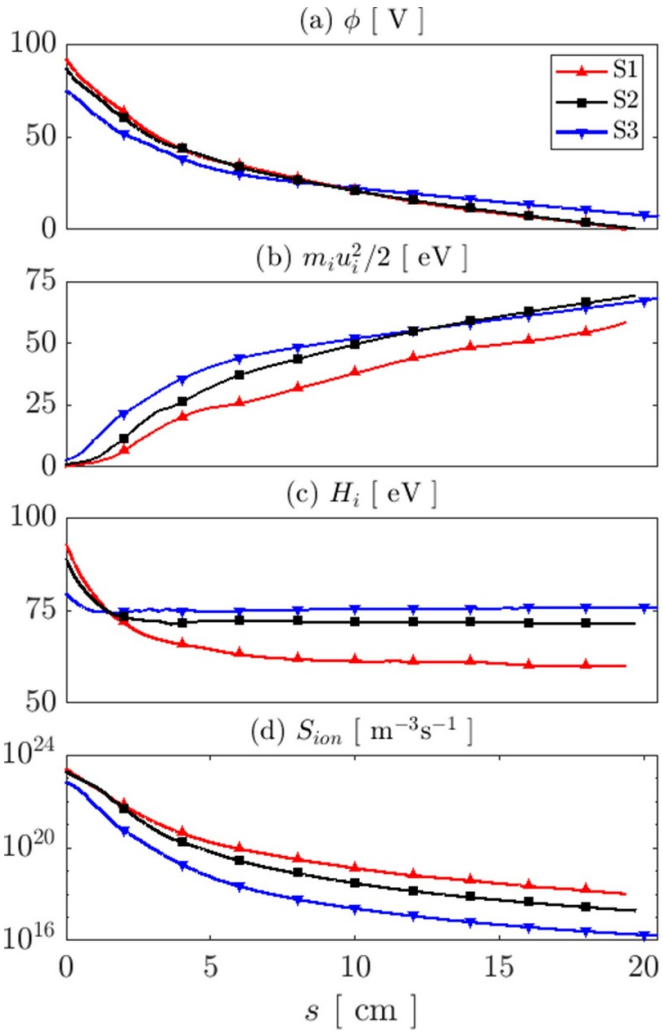

Figure 7. Evolution along streamlines S1 (red), S2 (black), and S3 (blue) shown in figure 1(a) of (a) the electrostatic potential, (b) the Xe^+ kinetic energy, (c) the Xe^+ mean total energy and (d) ionization source, for the case with $\alpha_t = 0.05$.

the presence of the lower energy ion population in figure 5. Overall, ions moving along streamlines with higher divergence angles feature a smaller drop in their mean total energy as ionization becomes insignificant earlier in the acceleration. Finally, observe that further downstream (roughly from $s = 10$ cm onward) the ionization rate has decreased to a point that H_i remains essentially constant on all streamlines, as corresponds with the near-collisionless behavior.

3.3. Thruster performance

Table 2 shows the comparison of experimental thruster performance and other figures of merit with their numerical estimations.

Numerically, thrust is computed as the sum $F = \sum F_l$ of the momentum flux of each species l through the free boundaries of the domain S_f,

$$F_l = \int_{S_f} 1_z \cdot (m_l n_l \boldsymbol{u}_l \boldsymbol{u}_l + \bar{\bar{P}}_l) \cdot \mathbf{1}_n \mathrm{d}A, \tag{3}$$

where dA is the area element, $\mathbf{1}_n$ the outward normal vector, and $\bar{\bar{P}}_l$ the pressure tensor of species l. Specific impulse is then defined as

$$I_{sp} = \frac{F}{\dot{m} g_0}, \tag{4}$$

where g_0 is the standard gravity constant at sea level, and the thrust efficiency is computed in terms of the absorbed power as

$$\eta_F = \frac{F^2}{2\dot{m} P_a}. \tag{5}$$

It is noted that the trend is toward lower numerical values of F, I_{sp} and η_F for increasing values of α_t. Simulations overpredict the thrust value and derived quantities such as the specific impulse and thrust efficiency with respect to the experimental measurements for all values of α_t. This disagreement is likely due to limitations in the current model. In particular background pressure, present in the experiments and not in the simulations, can affect thrust measurements of EP devices. Previous works [42] have reported a decrease in thrust measured from 800 to 400 μN for an increase in background pressure from 10^{-7} to 10^{-5} mbar-Xe. A background pressure of the order of $3\text{–}4\times10^{-6}$ mbar-Xe is measured at the ONERA-B09 facility during thruster operation. This value lies within the range of values reported modifying ECR performance in the previous ECRT experiments mentioned. Thus, it can be expected that thrust value measured in perfect vacuum conditions (i.e. free space), which represents the simulated case, would be larger than the one obtained in the current experimental conditions.

Moreover, the equivalent Xe neutral density corresponding to the measured background pressure around $3\text{–}4\times10^{-6}$ mbar-Xe is 0.7 to 1×10^{17} m^{-3}. In the simulations, Xe neutral density in the range of $10^{17} > n_n > 10^{16}$ m^{-3} for $5.8 < z < 15.3$ cm is found at the axis. The larger background pressure is expected to alter the collisions along the plume, specially electron-neutral collisions [15], and also the plasma expansion along the magnetic nozzle. Therefore, the inclusion of the background pressure effect in the simulations may lower thruster performance.

The numerical ion beam current in table 2 is computed using equation (2) with the ion current density profile at $\rho = 13.5$ cm in order to match the maximum angle accessed by measurements (i.e. 70°). In order to have a rough estimate of the error of this approximation, it is verified that for all the simulation cases I_b at $\rho = 13.5$ cm matches the values obtained at $\rho = 16$ cm. A good agreement is found between the numerical and the experimental ion beam current.

Three other figures are compared between numerical and experimental results. First, the utilization efficiency

$$\eta_u = \frac{\dot{m}_{ib}}{\dot{m}}, \tag{6}$$

where $\dot{m}_{ib}$ represents the total ion beam flow rate downstream, and $\dot{m}$ the injected neutral mass flow rate. Second, the energy efficiency defined as

Table 2. Thruster performance figures measured experimentally and obtained in the three simulations with $\alpha_t = 0.035$, 0.05 and 0.08. The ion beam current is computed with a maximum angle of 70°. The maximum T_e measurement is taken at $z = 10$ cm (indicated with *), while the numerical maximum T_e refers to global values.

	Case	Exp.	0.035	0.05	0.08
F (μN)	Thrust	601 ± 15	934	877	781
I_{sp} (s)	Specific impulse	312 ± 8	484	455	405
η_F (%)	Thrust efficiency	3.1 ± 0.2	7.4	6.5	5.2
I_b (mA)	Ion beam current	62 ± 3	67	62	56
η_u (%)	Utilization efficiency	43 ± 2.1	47.1	44.4	40.7
η_{en} (%)	Energy efficiency	13.4 ± 0.6	15.7	15.5	13.7
$\psi_{90\%}$ (°)	90%-current angle	60 ± 1	58	60	61
$E_{i,max}$ (eV)	Maximum E_i	65	71	75	74

$$\eta_{en} = \frac{I_b E_{i,max}}{P_a}, \tag{7}$$

where $E_{i,max}$ is the peak ion energy of the IEDF. Third, the 90% divergence angle $\psi_{90\%}$, which is defined as the cone where 90% of the total ion beam current is collected:

$$\pi\rho^2 \int_{-\psi_{90\%}}^{\psi_{90\%}} j_i(\psi) \sin(|\psi|)\, d\psi = 0.9 I_b\,. \tag{8}$$

Overall, good agreement is found as well in these three figures of merit, and the weak trend observed with increasing α_t is toward lower utilization and energy efficiency, and higher beam divergence. A value around $\alpha_t = 0.05$ yields a good fit with the experimental results in this regard.

3.4. Electrostatic potential and electron temperature

Angular and axial LP measurements of electrostatic potential ϕ and electron temperature T_e are shown in figure 8. The reference potential ϕ^* is taken at $\rho = 16$ cm, $\psi = 0$ deg. The angular profile of ϕ exhibits a valley around the centerline, which seems to originate in the wake of the metallic rod in the plasma source. In contrast, the measured angular profile of T_e is essentially flat. Small asymmetries on both variables may be attributed to experimental uncertainties. The electrostatic potential decreases along the axis, consistently with a plasma expansion. The electron temperature also decreases, indicating the existence of electron cooling in the downstream direction, dropping from 10.7 to 5.2 eV in 10 cm. Both variables decrease with a slower rate farther downstream.

Figure 8 also displays the comparison with numerical results for $\alpha_t = 0.035$, 0.05, 0.08. The electrostatic potential also displays a valley around the axis, but is flatter within the central part of the plume than the experiments, until roughly $\psi = 20°$; beyond that angle, it increases gradually toward the plume periphery, similarly to what is measured experimentally. The axial behavior rate of ϕ agrees well with the experimental results and no differences are observed between the different α_t cases.

In the simulations, the electron temperature features a maximum about the centerline, along the magnetic lines where most microwave power absorption is observed in the model [19], which is not observed experimentally. This peak decreases as α_t is increased. Along the ρ direction, the model is near-isothermal, differing from the experimentally-observed electron cooling. Indeed, the behavior of T_e in the simulations is consistent with the heat flux closure relation used, detailed in [21], in which parallel conductivity is much larger than perpendicular (cross-field) conductivity. These discrepancies may suggest that the anomalous transport coefficient in the momentum equation and in the energy equation need to be different. Moreover, a full kinetic treatment of electrons may be needed to correctly model electron cooling in the near-collisionless plume [43–46].

While in the works just cited it is argued that polytropic closure relations of the form $T_e \propto n_e^{\gamma-1}$ are not theoretically justified for a near-collisionless plasma expansion in a magnetic nozzle, this approach has been used in the past to account approximately for electron cooling in plume expansions [9, 47, 48], and nevertheless it is instructive to estimate the effective polytropic exponent γ of the expansion, as a first measure of the cooling rate in the plume. From the axial experimental results, γ is equal to 1.34 ± 0.04, a value which is close to others obtained in the past [49]. This value can be used with the numerical electron density axial profiles and the initial value of T_e to project the corresponding cooling behavior in the model for the different α_t cases, as shown in figure 8(d). While this last computation is not self-consistent, it evidences that a better agreement with the axial T_e measurements may be achieved once an improved electron cooling model is implemented into the model.

On the one hand, the near-flat angular profile of T_e measured suggests that either the radial power absorption profile at the ECR surface differs substantially from the one reproduced by the model, or that a much higher perpendicular mobility exists for electrons in the source region of the ECRT. Indeed, as evidenced in figure 8(b), larger cross-field diffusion α_t leads to a flatter T_e angular profile, and smaller maximum value of T_e (see also table 2). This suggests that a non-homogeneous map of α_t may be needed to reproduce the experimental results.

Lastly, we note that the electrostatic field map and the meridian electron currents may depend on the position and nature of the boundary conditions (here dielectric conditions both in the experiment and in the simulation). The analysis of the effect of other alternative boundary conditions remains open to future studies.

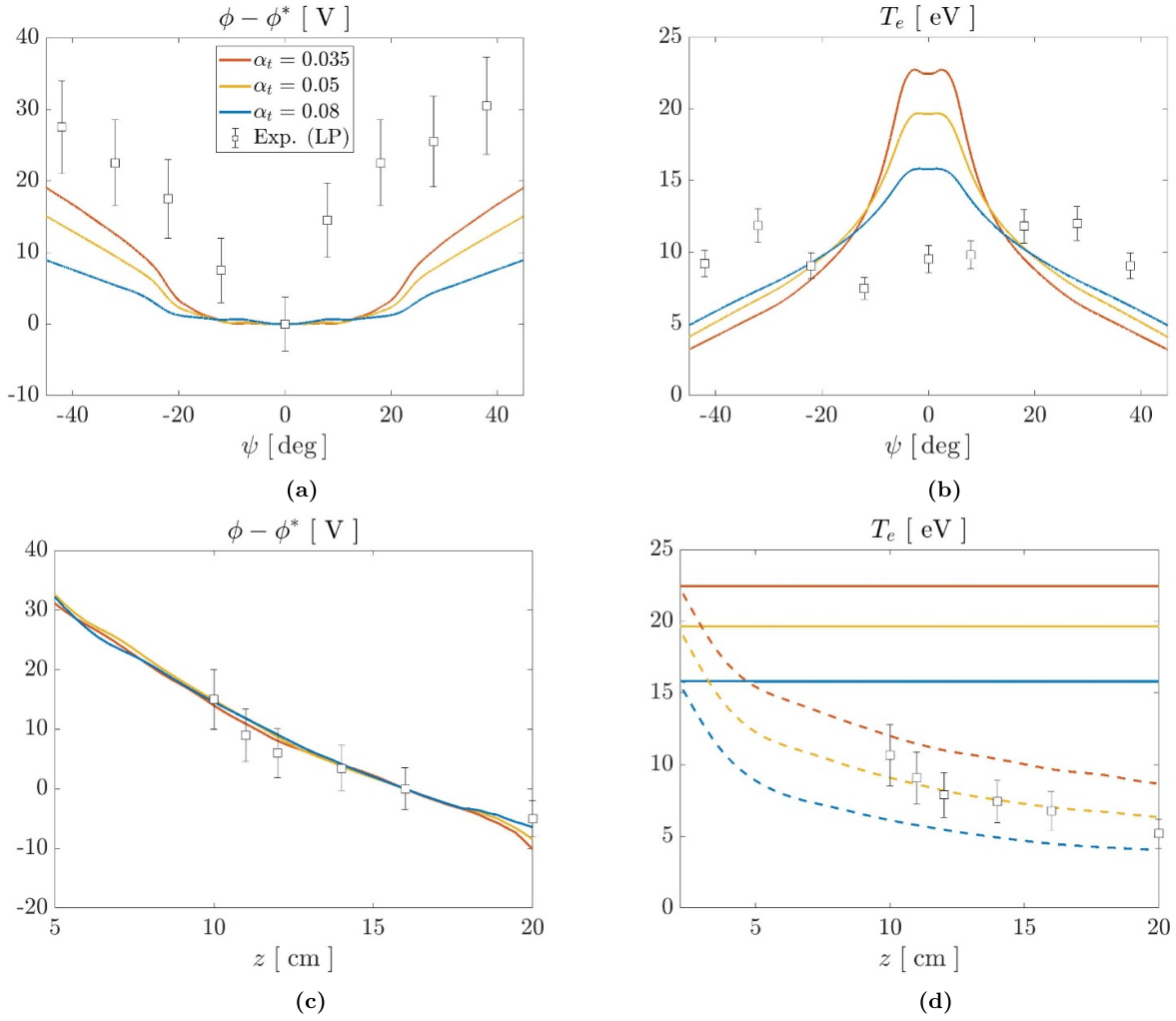

Figure 8. Comparison of LP measurements (scatter symbols) to model results (solid lines) of (a) angular profile of electrostatic potential (b) angular profile of electron temperature, and similarly for their respective axial profiles in (c) and (d). The reference electrostatic potential (ϕ^*) is taken with respect to the experimental values at $z = 16$ cm $\psi = 0°$. In (d), dashed lines represent the expected projected polytropic electron cooling using the experimental polytropic coefficient and the numerical electron density, as explained in section 3.4.

4. Conclusions

Experimental angular and axial probe measurements of ion current density, electron density, electron temperature, and electrostatic potential, as well as thrust measurements, have been compared with self-consistent numerical simulations of an ECRT prototype, which integrate the slow plasma dynamics and the fast electromagnetic fields. Effort has been put into experimentally reproducing the thruster setup and operating conditions used in the numerical simulations, in particular by adding a dielectric coating inside the thruster chamber to favor the comparison with numerical dielectric boundary conditions. The main goal of this study was to benchmark the numerical model of this device. This work is part of the ongoing endeavor toward the improvement and validation of our current understanding of the phenomena involved in this thruster operation, essential for an optimization of the technology.

The presented results show a reasonable to good agreement between the model and the experimental data, although only for some variables, and for certain values of the coefficient α_t used to model anomalous transport. Ion current density, electron density and electrostatic potential are properly captured by the model, both in the angular and axial directions. An annular-shaped plasma profile is seen to form in the source region in the model due to the presence of the central antenna pole, which gradually evolves into a single-peaked profile downstream. The electron density expansion in the far plume is underestimated by the model, which also predicts a flat electrostatic potential until roughly $\psi = \pm 20°$ which is not observed experimentally. Values of the ion beam current, utilization and energy efficiencies, and the 90%-current angle are found in good agreement with experiments, specially for the case with $\alpha_t = 0.05$. Simulations overestimate thrust, and therefore also specific impulse, thrust efficiency, and, to a minor degree, the peak Xe^+ energy in the plume.

While the present work represents a partial validation of the model, a full, direct validation is hindered by the inherent limitations of experimental measurements, namely (1) the error associated to probe measurements, (2) the inability to bring the electrostatic probes too close to the thruster ionization

chamber without introducing an excessive perturbation, (3) the influence of background pressure on the magnetic nozzle expansion, and (4) the effect of wall coating ageing on the repeatability of the measurements.

On the other hand, numerical simulations are limited by the available computational resources, which forbid extending the simulation domain too far. It has been shown that the cross-field plasma transport is larger than the one predicted by classical models, and that some form of enhanced (anomalous) transport is needed to correctly reproduce the plasma and thrust measurements. The present work has explored this matter with a simple, phenomenological, uniparametric anomalous transport model, which lowers the effective Hall parameter in the plasma, finding that values of $\alpha_t \simeq 0.05$ adequately reproduce the behavior found in the measurements. While the mechanisms (e.g. instabilities) leading to anomalous transport in HETs and ECRTs may differ substantially, the application of this model to the present case is justified here as a first approach to control cross-field transport, aiming to facilitate the fitting of the numerical results to the experimental measurements. To our knowledge, this is one of the first works to explore the effects of anomalous transport in ECRT simulations, even if the model used (based on HET modeling heritage) may only be considered a first empirical approximation for these devices.

Evidently, the development of accurate models of anomalous transport in ECRTs requires a dedicated investigation, and is outside of the scope of the present work. More advanced anomalous transport models are needed to properly reproduce the complexities of their physics and this constitutes an open area of research. Measurements closer to the ionization chamber with non perturbative diagnostics would bring interesting insight to challenge the uniparametric anomalous transport hypothesis and refine the understanding of anomalous transport in ECRTs. Furthermore, simulations here suggest that anomalous diffusion coefficients for particle and energy diffusion are likely different.

The comparison has also enabled the identification of key areas of improvement of the model. Firstly, the electron heat flux closure relation presently employed must be corrected, and possibly incorporate the latest kinetic modeling results [45, 46], to accurately predict the observed electron cooling along the magnetic nozzle. Secondly, boundary conditions must be designed carefully to better represent the expansion of a plasma plume to infinity. Thirdly, background pressure and other facility effects could be included in the model, as this would lead to a better understanding of their influence on the measurements. This will also be an interesting tool to facilitate the vacuum-chamber to in-flight data comparison and improve the understanding of the effect of the test facilities on the measured performance on ground.

Data availability statement

The data that support the findings of this study are available upon reasonable request from the authors.

Acknowledgments

The initial part of this research has been funded by the European Union H2020 program under Grant Agreement 730028 (Project MINOTOR). Subsequent funding of the EP2 research team came from the ESPEOS project, funded by Agencia Estatal de Investigación (PID2019-108034RB-I00/AEI/10.13039/501100011033). Sánchez-Villar's funding came from Spain's Ministry of Science, Innovation and Universities, under Grants FPU17/06352 and EST/00696. Also, Sánchez-Villar thanks ONERA's research team for supporting this project and for hosting him during his research stay (April–June 2021) at their facilities.

ORCID iDs

Álvaro Sánchez-Villar https://orcid.org/0000-0003-3727-9319
Federico Boni https://orcid.org/0000-0002-8977-8593
Victor Désangles https://orcid.org/0000-0001-7557-2271
Julien Jarrige https://orcid.org/0000-0003-1365-6044
Denis Packan https://orcid.org/0000-0002-0923-9769
Eduardo Ahedo https://orcid.org/0000-0003-2148-4553
Mario Merino https://orcid.org/0000-0001-7649-3663

References

[1] Charles C, Boswell R and Lieberman M 2006 Xenon ion beam characterization in a helicon double layer thruster *Appl. Phys. Lett.* **89** 261503
[2] Navarro-Cavallé J, Wijnen M, Fajardo P and Ahedo E 2018 Experimental characterization of a 1 kw helicon plasma thruster *Vacuum* **149** 69
[3] Diaz F 2000 The Vasimr rocket *Sci. Am.* **283** 90
[4] Crimi G, Eckert A and Miller D 1967 Microwave driven magnetic plasma Accelerator Studies (Cyclops), *Technical Report* (General Electric Company, Space Sciences Laboratory, Missile and Space Division)
[5] Kosmahl H G, Miller D B and Bethke G W 1967 Plasma acceleration with microwaves near cyclotron resonance *J. Appl. Phys.* **38** 4576
[6] Sercel J 1987 Electron-cyclotron-resonance (ECR) plasma acceleration *AIAA 19th Fluid Dynamics, Plasma Dynamics and Lasers Conf.*
[7] Jarrige J, Elias P, Cannat F and Packan D 2013 Performance comparison of an ECR plasma thruster using argon and xenon as propellant gas *33rd Int. Electric Propulsion Conf. (Washington, DC, 7–10 October)* (Fairview Park, OH: Electric Rocket Propulsion Society) p 2013-420
[8] Cannat F, Jarrige J, Lafleur T, Elias P and Packan D 2015 Experimental geometry investigation of a coaxial ECR plasma thruster *Proc. 34th Int. Electric Propulsion Conf. (Kobe-Hyogo, Japan)* p 2015-242
[9] Lafleur T, Cannat F, Jarrige J, Elias P Q and Packan D 2015 Electron dynamics and ion acceleration in expanding-plasma thrusters *Plasma Sources Sci. Technol.* **24** 65013
[10] Vialis T, Jarrige J, Aanesland A and Packan D 2018 Direct thrust measurement of an electron cyclotron resonance plasma thruster *J. Propuls. Power* **34** 1323
[11] Peterschmitt S and Packan D 2019 Comparison of waveguide coupled and coaxial coupled ECRA magnetic nozzle thruster using a thrust balance *IEPC 2019*

[12] Correyero S, Jarrige J, Packan D and Ahedo E 2019 Plasma beam characterization along the magnetic nozzle of an ECR thruster *Plasma Sources Sci. Technol.* **28** 095004
[13] Peterschmitt S and Packan D 2021 Impact of the microwave coupling structure on an electron-cyclotron resonance thruster *J. Propuls. Power* **37** 806
[14] Wachs B and Jorns B 2019 Technique for two-frequency optimization of an ECR magnetic nozzle thruster *Int. Electric Propulsion Conf.* p 1
[15] Wachs B and Jorns B 2020 Background pressure effects on ion dynamics in a low-power magnetic nozzle thruster *Plasma Sources Sci. Technol.* **29** 045002
[16] Hepner S, Wachs B and Jorns B 2020 Wave-driven non-classical electron transport in a low temperature magnetically expanding plasma *Appl. Phys. Lett.* **116** 263502
[17] Peterschmitt S, Porto J C, Elias P-Q and Packan D 2019 A diffusion model in velocity space to describe the electron dynamics in an ECR plasma thruster with magnetic nozzle *EUCASS 2019 (MADRID, Spain)*
[18] Cannat F, Lafleur T, Jarrige J, Chabert P, Elias P and Packan D 2015 Optimization of a coaxial electron cyclotron resonance plasma thruster with an analytical model *Phys. Plasmas* **22** 053503
[19] Sánchez-Villar Á, Zhou J, Ahedo E and Merino M 2021 Coupled plasma transport and electromagnetic wave simulation of an ECR thruster *Plasma Sources Sci. Technol.* **30** 045005
[20] Domínguez-Vázquez A, Zhou J, Fajardo P and Ahedo E 2019 Analysis of the plasma discharge in a Hall thruster via a hybrid 2D code *36th Int. Electric Propulsion Conf.* (Vienna, Austria: Electric Rocket Propulsion Society) p IEC-2019-579
[21] Domínguez-Vázquez A 2019 Axisymmetric simulation codes for Hall effect thrusters and plasma plumes *PhD Thesis* Universidad Carlos III de Madrid, Leganés, Spain
[22] Perales-Díaz J, Domínguez-Vázquez A, Fajardo P, Ahedo E, Faraji F, Reza M and Andreussi T 2022 Hybrid plasma simulations of a magnetically shielded Hall thruster *J. Appl. Phys.* **131** 103302
[23] Stix T H 1992 *Waves in Plasmas* (New York: American Institute of Physics)
[24] Sánchez-Villar A and Merino M 2018 Advances in wave-plasma modelling in ECR thrusters *Space Propulsion Conf. 2018* (Seville: Association Aéronautique et Astronautique de France) p 00346
[25] Greenwood A and Jin J 1999 A novel efficient algorithm for scattering from a complex BOR using mixed finite elements and cylindrical PML *IEEE Trans. Antennas Propag.* **47** 620
[26] Fife J 1998 Hybrid-PIC modeling and electrostatic probe survey of Hall thrusters *PhD Thesis* Massachusetts Institute of Technology
[27] Parra F, Ahedo E, Fife J and Martínez-Sánchez M 2006 A two-dimensional hybrid model of the Hall thruster discharge *J. Appl. Phys.* **100** 023304
[28] Mikellides I and Katz I 2012 Numerical simulations of Hall-effect plasma accelerators on a magnetic-field-aligned mesh *Phys. Rev.* E **86** 046703
[29] Cannat F, Lafleur T, Jarrige J, Chabert P, Elias P-Q and Packan D 2015 Optimization of a coaxial electron cyclotron resonance plasma thruster with an analytical model *Phys. Plasmas* **22** 053503
[30] Peterschmitt S 2020 Development of a stable and efficient electron cyclotron resonance thruster with magnetic nozzle *PhD Thesis* Institut Polytechnique de Paris
[31] Jarrige J, Elias P-Q, Cannat F and Packan D 2013 Performance comparison of an ECR plasma thruster using argon and xenon as propellant gas *33rd Int. Electric Propulsion Conf.* p IEC-2013-420
[32] Boni F, Jarrige J, Désangles V and Minea T 2021 The curling probe: a numerical and experimental study. Application to the electron density measurements in an ECR plasma thruster *Rev. Sci. Instrum.* **92** 033507
[33] Druyvesteyn M J and Penning F M 1940 The mechanism of electrical discharges in gases of low pressure *Rev. Mod. Phys.* **12** 87
[34] Brown D L, Walker M L R, Szabo J, Huang W and Foster J E 2017 Recommended practice for use of Faraday probes in electric propulsion testing *J. Propuls. Power* **33** 582
[35] Lobbia R B and Beal B E 2017 Recommended practice for use of Langmuir probes in electric propulsion testing *J. Propuls. Power* **33** 566
[36] Pérez-Grande D, Gonzalez-Martinez O, Fajardo P and Ahedo E 2016 Analysis of the numerical diffusion in anisotropic mediums: benchmarks for magnetic field aligned meshes in space propulsion simulations *Appl. Sci.* **6** 354
[37] Marks T A, Mikellides I G, Lopez Ortega A and Jorns B 2020 Hall2de simulations of a magnetic nozzle *AIAA Propulsion and Energy 2020 Forum* p 3642
[38] MFEM: modular finite element methods library (available at: http://mfem.org)
[39] Peterschmitt S and Packan D 2019 Comparison of waveguide coupled and coaxial coupled ECRA magnetic nozzle thruster using a thrust balance *36th Int. Electric Propulsion Conf. (15–20 September 2019)* (Austria: University of Vienna)
[40] Charles C 2010 High density conics in a magnetically expanding helicon plasma *Appl. Phys. Lett.* **96** 051502
[41] Lxcat database (available at: https://nl.lxcat.net) (Accessed 21 October 2019)
[42] Holste K *et al* 2020 Ion thrusters for electric propulsion: scientific issues developing a niche technology into a game changer *Rev. Sci. Instrum.* **91** 061101
[43] Martínez-Sánchez M, Navarro-Cavallé J and Ahedo E 2015 Electron cooling and finite potential drop in a magnetized plasma expansion *Phys. Plasmas* **22** 053501
[44] Ahedo E, Correyero S, Navarro J and Merino M 2020 Macroscopic and parametric study of a kinetic plasma expansion in a paraxial magnetic nozzle *Plasma Sources Sci. Technol.* **29** 045017
[45] Zhou J, Sánchez-Arriaga G and Ahedo E 2021 Time-dependent expansion of a weakly-collisional plasma beam in a paraxial magnetic nozzle *Plasma Sources Sci. Technol.* **30** 045009
[46] Merino M, Nuez J and Ahedo E 2021 Fluid-kinetic model of a propulsive magnetic nozzle *Plasma Sources Sci. Technol.* **30** 115006
[47] Dannenmayer K, Mazouffre S, Merino M and Ahedo E 2012 Hall effect thruster plasma plume characterization with probe measurements and self-similar fluid models *48th AIAA/ASME/SAE/ASEE Joint Propulsion Conf. & Exhibit (30 July–1 August)* (*Atlanta, GA*: American Institute of Aeronautics and Astronautics) p AIAA-2012-4117
[48] Cichocki F, Merino M and Ahedo E 2014 Modeling and simulation of EP plasma plume expansion into vacuum *50th AIAA/ASME/SAE/ASEE Joint Propulsion Conf. & Exhibit (28–30 July)* (Cleveland, OH: American Institute of Aeronautics and Astronautics) p AIAA-2014-3828
[49] Correyero S, Jarrige J, Packan D and Ahedo E 2019 Plasma beam characterization along the magnetic nozzle of an ECR thruster *Plasma Sources Sci. Technol.* **28** 095004